scientific reports

Check for updates

OPEN

Plasmon-enhanced visible photodetectors based on hexagonal boron nitride (hBN) with gold (Au), silver (Ag), and non-alloyed bimetallic (Au/Ag) nanoparticles

Muhammad Nur Syafiq Mohamad Ismail[1,2], Muhammad Aiman Saufi Ahmad Fahri[2], Chee Leong Tan[1,3]✉ & Rozalina Zakaria[2]✉

Two-dimensional (2D) hexagonal boron nitride (hBN) has garnered significant attention due to its exceptional thermal and chemical stability, excellent dielectric properties, and unique optical characteristics, making it widely used in deep ultraviolet (DUV) applications. However, the integration of hBN with plasmonic materials in the visible region (532 nm) has not been fully explored, particularly in terms of morphology regulation and size control of mono- and bimetallic nanoparticles (BMNPs) namely gold (Au), silver (Ag) and Au-Ag. A Schottky junction-based metal–semiconductor contact configuration is employed to achieve hot-carrier reflections on the metal side, enhancing the quantum efficiency of the photodetector. The fabricated metallic NPs/hBN photodetector demonstrates a responsivity of 1.33 A/W, a specific detectivity of 1.03×10^{11} Jones, an ultra-low dark current of 7.00 µA and a high photo response ratio of 2.47. This improved performance is attributed to the visible light-modulated band-to-band excitation in hBN layer and internal photoemission resulting from the NPs/hBN junction. The device also exhibits a rapid response speed of less than 300 µs for all the devices. This approach of integrating 2D/metal opens possibilities for fabricating low-cost, high-performance, flexible photodetectors for a range of optoelectronic devices.

Keywords Hexagonal boron nitride (hBN), Plasmonic enhancement, Metallic nanoparticles, Visible light photodetector, External quantum efficiency (EQE)

The engineering of material heterostructures using two-dimensional (2D) materials has attracted significant attention for applications in optoelectronic devices, energy, and beyond. Hexagonal boron nitride (hBN), a 2D insulator with a bandgap of approximately 6 eV, offers an atomically smooth surface, exceptional chemical stability, and high optical transparency in the visible spectrum[1,2]. Hexagonal boron nitride (hBN) has indeed emerged as a significant two-dimensional (2D) material, akin to graphene, due to its minimal lattice mismatch and ability to maintain high carrier mobility. Moreover, hBN has unique properties in the deep ultraviolet (DUV) and infrared (IR) wavelength bands owing to its indirect bandgap structure and hyperbolic phonon polaritons (HPPs)[3]. hBN is a wide bandgap semiconductor material which known for its high thermal conductivity and chemical inertness. Notably, hBN layers have a honeycomb lattice structure based on sp^2 hybridization[4], where the surface of hBN is atomically smooth, free of dangling bonds and charge-trapping sites[5]. Therefore, it has attracted considerable interest as an ideal substrate for forming van der Waals (vdW) heterostructures with other materials[5]. hBN is a layered structure where boron and nitrogen atoms are bound by strong covalent bonds in each layer. hBN is composed of boron (a group III element) and nitrogen (a group V element), which form

[1]College of Integrated Circuit Science and Engineering, Nanjing University of Posts and Telecommunications, Nanjing 210023, China. [2]Photonics Research Centre, Universiti Malaya, Kuala Lumpur 50603, Malaysia. [3]Guangdong Greater Bay Area Institute of Integrated Circuit and System, Guangzhou 510535, China. ✉email: cheelong@njupt.eu.cn; rozalina@um.edu.my

strong ionic bonds. This ionic character contributes to its stability and affects its optical properties, including its wide band gap and phonon interactions[6–8].

In short-wave light-emitting diodes (LEDs), hBN serves as a highly effective substrate material, enabling the efficient emission of ultraviolet (UV) and visible light while maintaining excellent thermal conductivity and stability under high-power conditions[9]. The strong electron-phonon interactions facilitate effective radiative recombination processes, allowing for potential applications in DUV light-emitting devices[10,11]. hBN exhibits significant excitonic emission due to its unique electronic structure. The excitons in hBN are characterized by a strong binding energy of approximately 300 meV, which allows for efficient photon emission even at UV wavelengths. This high binding energy is particularly advantageous as it enables stable excitonic states at room temperature, enhancing the potential for practical applications in DUV devices[12].

hBN can be used to create hybrid 2D heterostructures with metals (such as Au or Ag), enhancing the light-matter interaction at the metal surface where SPR occurs. This combination can potentially increase the coupling efficiency where the plasmon energy-momentum dispersion of bulk hBN has been studied before[13]. Localized surface plasmon resonance (LSPR) of noble metal nanostructures, has been considered an effective way for enhancing the performance of optoelectronic devices where metallic nanostructures have much attracted in the past decade due to its strong plasmon resonance on photonics and sensing application; such in photocatalysis, optical sensing, and optoelectronics[14–16]. This metallic NPs strongly absorb light due to the SPR behavior, which can be tuned by varying the size, shape, interparticle coupling, and surroundings[17–21]. It is also providing a strong magnitude of electromagnetic fields near the nanostructures compared to the incident light that gives rise to the LSPR. Those manipulations include the use of single monometallic nanoparticles (NPs), bimetallic non-alloyed nanoparticles (BMNPs), and bimetallic alloy nanoparticles[22–24]. SPR happens when the frequency of the incident lights shows resonance with the oscillation of NPs, which arises in light absorption and scattering[25]. Thus far, the most typically used materials for plasmonic applications are gold (Au) and silver (Ag) owing to their low intrinsic loss.

Plasmonic-empowered photodetectors have been achieved up to IR and visible frequencies, but rarely in the UV regime[26] where size of particles also plays a role in manipulating the SPR peaks, where bigger particles gives rise to redshift[27]. These tunability properties of SPR peaks for Au and Ag make them suitable for most photosensor applications in visible regions. However, single monometallic nanoparticles such as Au and Ag have narrow SPR peaks and thus have limitations in wide-range of photosensor applications[28]. Due to this, bimetallic nanoparticles have emerged to achieve broader SPR peaks, increased carrier density, longer carrier lifetime, and better stability against oxidation. The use of bimetallic materials in photodetectors can lead to significant enhancements in performance metrics such as responsivity, detectivity, and speed due to better light-matter interactions and plasmonic resonance effects particularly those utilizing Au-Ag nanoparticles improve sensitivity and significant enhancement in light absorption for UV, visible, and near IR photodetection applications[29–33].

To achieve the optimized performance of the photodetector, the combination of plasmonic materials with 2D materials must be elaborately designed to realize the desired enhancement effect. Placing 2D materials next to plasmonic nanostructures leads to a significant increase in light intensity, which in turn enhances the absorption coefficient of the 2D materials. Over the past years, the effective improvement of light-matter interaction in various 2D material photodetectors by metal nanostructure layers has been proven, including an extensive material family such as graphene[34,35], MoS_2[36,37], WS_2[38], BP[39], $MoTe_2$[40] and many more. The near-field enhancement undoubtedly improves light absorption in 2D material layers, normally accompanied by the injection of plasmonic hot carrier injection[40]. Lin Gao et al.[41]. reported that the Schottky barrier and trap state between metal-semiconductor structures would decrease carrier collection efficiency, where the performance improved the photocurrent gain and reduced the dark current. At 1 V positive bias and 3.9 nW illumination power, the responsivity of the Au–WS_2–Graphene–Au structure is as high as 29.0 A/W, which indicates that it has excellent ability in light response and weak light detection. Liu et al.[42] reported the photo response of a similar wavelength of 532 nm light as a photodetector delivers a high a specific detectivity of 3.9×10^9 Jones, responsivity of 0.06 A/W and an external quantum efficiency of 13.8%, with a rise and decay time being 110 and 120 ms, respectively, for solution-processed continuous nanoporous Au film of a CNAuF/TiO_2 Schottky junction.

This article presents a plasmonic photodetector based on hBN materials integrated with metallic nanoparticles (NPs) of Au, Ag, and Au/Ag at 532 nm light illumination. Experimental findings show a significant improvement in photoresponse across all devices (Au-hBN, Ag-hBN, Au/Ag-hBN with our photodetector demonstrating excellent performance and high responsivity at room temperature.

Methodology

Formation of AuNPs, AgNPs, and Au/AgNPs

The Glass (Sail Brand No.7101) substrates were cleaned by sonication using an ultrasonic cleaning machine for 5 min at 25 °C with each solvent starting with acetone solution, isopropyl alcohol, and distilled water before drying using the spray gun. Thin Au and Ag films were prepared using the electron beam evaporation deposition technique. The films were deposited under the pressure of 9×10^{-6} Torr, a deposition rate of 0.1–0.3 Å/s and deposition voltage of 6.99 kV for better uniformity. The thickness of Au and Ag thin films were set at 8 nm and 10 nm, respectively. After the Au and Ag thin films were formed on the substrates, they were brought to undergo the dewetting process. The Au thin film undergoes a dewetting process at 600 °C for 1 min to obtain AuNPs, while the Ag thin film undergoes a dewetting process at 450 °C for 1 min to obtain the Ag NPs. The Au/Ag NPs were produced using the combination steps of producing the AuNPs and followed by AgNPs. The detailed parameters for the NPs fabrication are shown in Table 1.

Sample	Coating thickness (nm)	Annealing temperature (℃)	Annealing time (min)
Au	8	600	1
Ag	10	450	1
Au/Ag	8/10	600/450	1/1

Table 1. Detail parameters for the formations of au and ag nanoparticles.

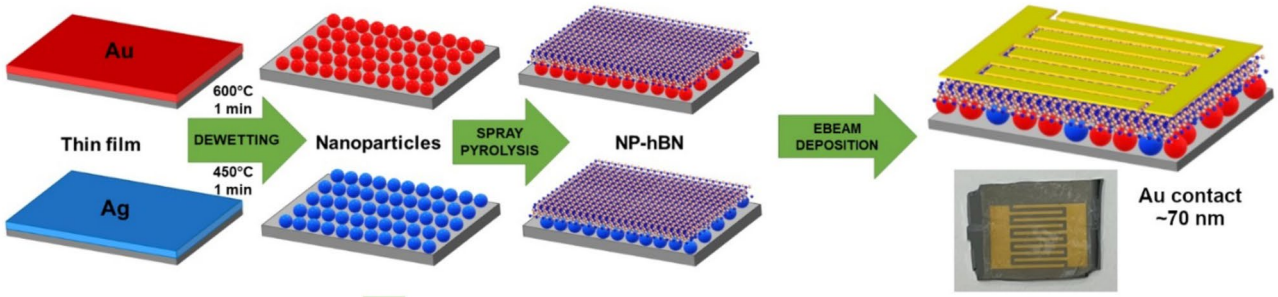

Fig. 1. Fabrication process of NPs-hBN photodetector from thin layer deposition, nanoparticles formation and Au contact for devices.

Fabrication of Au-hBN, Ag-hBN, and AuAg-hBN photodetector devices

Photodetectors were fabricated based on the scheme shown in Fig. 1. The hBN solution was prepared using the liquid phase exfoliation (LPE) technique. Initially, 54 ml of IPA and 126 ml of DI water (30:70 ratio) were mixed to form a solvent for the hBN powder. Then, 450 mg of hBN powder was mixed into the solvent to form an hBN dispersion solution with a 2.5 mg/ml concentration. Next, the dispersion solution was sonicated at 40 kHz for two and a half hours to exfoliate the bulk hBN into a few layers of hBN. After this process, the sonicated solution was centrifuged at 1000 rpm for 10 min to separate the exfoliated hBN from its unexfoliated form. The supernatant was extracted and centrifuged again at 3000 rpm for 10 min. The final supernatant was collected and used as hBN solution.

The Au-hBN, Ag-hBN, and AuAg-hBN photodetector devices were prepared using spray pyrolysis hBN solution technique onto those NPs/Si substrates under hotplate treatment at 200 °C. A control of 10 ml of hBN solution was sprayed on each sample at a fixed height of 20 cm above the samples and at a low rate to ensure the uniformity of the hBN flakes formed. Once the hBN/NPs/ Si nanohybrid structure was obtained, Au film contact at 70 nm thickness was deposited onto the structure with 5 nm of Cr in between using e-beam evaporation. The fabrications of the devices are shown in Fig. 1 where Au and Ag's thin layers were deposited using an electron beam evaporation process before undergoing the dewetting process of 600 °C and 450 °C for 1 min, respectively and photodetector illumination. The presence of metallic nanoparticles can introduce additional pathways for charge carrier recombination. If not properly managed, this can lead to decreased photodetection efficiency. The interaction between the generated excitons in hBN and the metallic NPs may not always be favourable, potentially resulting in non-radiative recombination losses that further degrade device performance.

The hBN layer was applied over the nanoparticles using a spray pyrolysis process, followed by placement in an electron beam machine for the deposition of Au contacts, with a thickness of around 70 nm. The Au contact has the total dimension of 10 mm × 15 mm consisting of five pairs of electrodes. Each electrode has the width and gap of 0.6 mm. The illumination of light used is at 532 nm.

In Fig. 2a shows the photodetector set-up for I-V measurements using a function generator and Keysight SMU. In contrast, Fig. 2b shows the photo response set-up using a power supply and oscilloscope. Figure 2c effectively demonstrates how the incorporation of gold nanoparticles into the hBN structure impacts its energy band gap, showcasing the potential for enhanced optical properties through plasmonic effects. The LSPR effect induced by AuNPs can effectively boost the scattering and absorption of light in this configuration which depending on NPs sizes. This optical energy is absorbed by nearby AuNPs, generating a strong electric field and increasing the absorption of the incident light by the hBN layer[43].

As the work function of AuNPs (~5.2 eV) is greater than the work function of hBN (5.1 eV), hence Schottky barrier is formed at the junction of AuNPs and hBN, as depicted in Fig. 2c. When metallic nanoparticles (such as gold or silver) are combined with hBN, a Schottky barrier is created at the metal-semiconductor interface. This barrier is essential for controlling the flow of charge carriers (electrons and holes) between the metal and the semiconductor material and promote better carrier mobility. Under illumination with a visible light source, photons excite electrons, resulting in band-to-band transitions. The electric field created by the Schottky junction, along with the applied external bias, aids in the efficient separation of the photogenerated charge carriers, leading to an increase in current. For Au-hBN, the Schottky barrier is relatively high due to the higher work function of Au (~ 5.1 eV). For Ag-hBN, the barrier is slightly lower, as Ag has a lower work function (~ 4.3 eV). For the bimetallic system, the barrier height is influenced by the effective work function of the alloy, which lies between that of Au and Ag. Hot electrons are generated in the plasmonic nanoparticles due to localized surface

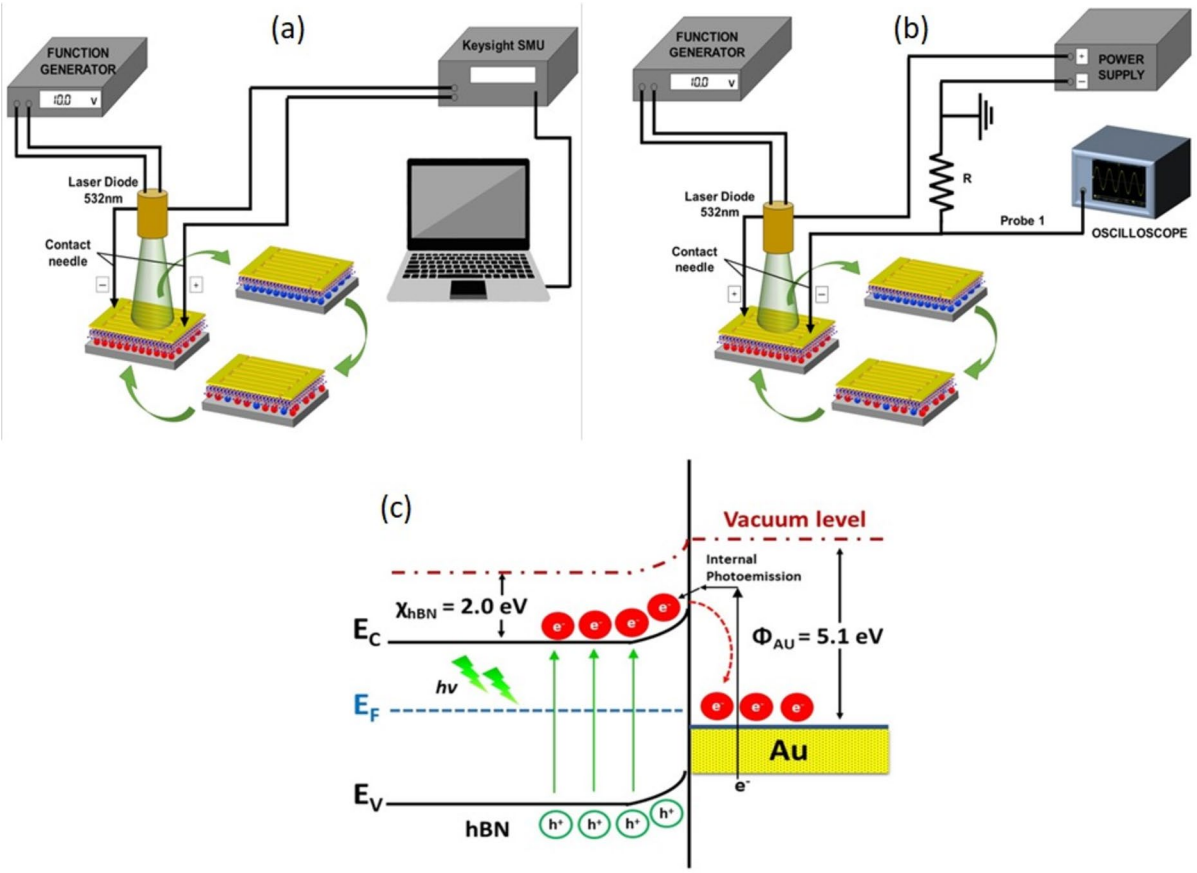

Fig. 2. Photodetector set-up for (**a**) I-V measurements and (**b**) photo response for all photodetector devices, and (**c**) schematic of the working mechanism of the fabricated photodetector where shows the photo-induced charge carriers, hot electrons generated in AuNPs as one of the devices and transferring to the hBN structure.

plasmon resonance (LSPR).These electrons must have sufficient energy to overcome the Schottky barrier and be injected into the conduction band (CB) of hBN. Since there are no holes available on the metal side, charge recombination is prevented as electrons pass through the Au-hBN interface, contributing to the high values of responsivity and external quantum efficiency (EQE). Internal photoemission occurs as electrons flow from Au into CB of hBN, supplying additional electrons and further enhancing the responsivity of the device. The hot electron in the LSPR will have sufficient energy to cross the Schottky barrier of the NPs and hBN junction, increasing the number of electrons where hBN will act as an electron acceptor, while the NPs will be the electron donor to create the charge transfer between the layers and promote charge carrier recombination[37].

Results and discussion

Physical and optical analysis

The FEI Quanta 400 F field effect scanning electron microscope (FESEM) was used to analyze the morphology structures. Images were processed using ImageJ and Origin to analyze the size of the particle's distribution as shown in Fig. 3. In Fig. 3a as for AuNPs, the analysis shows an average size of 75 nm, while for Fig. 3b for AgNPs, the average size is 60 nm. The AgNPs show more spherical and uniform particles than AuNPs, which have larger and elongated particles. In addition, the gold nanoparticles (AuNPs) exhibit a broader particle size range within the sample compared to silver nanoparticles (AgNPs), which demonstrate a more uniform particle size distribution throughout the sample.

Figure 3c shows that the Au/AgNPs were formed and segregated throughout the sample, not clumps and aggregated, which can be distinguished by particle sizes as the AuNPs exhibit larger particles than AgNPs. The Au/AgNPs also have vast particle sizes throughout the sample due to the presence of both AuNPs and AgNPs. Figure 3d shows EDX spectra for AuNPs and AgNPs where sizes are tabulated in Table 2.

Figure 4a shows the FESEM images of the formation of hBN with nanoflake structures, which are aggregated and dispersed throughout the sample. Figure 4b depicts the formation of hBN nanoflakes onto the AuNPs. The EDX spectra exhibit higher peaks of Au, B, and N elements, showing high purity of the depositing elements. The Perkin Elmer Lambda 750 UV-Vis Spectrometer was used to analyze the UV-Vis spectra for all configuration ranging from 200 nm to 800 nm of wavelength, as shown in Fig. 4c. The Au-hBN device shows an SPR peak at 544 nm, while the Ag-hBN device exhibits an SPR peak at 448 nm. For the Au/Ag-hBN device, the SPR peak

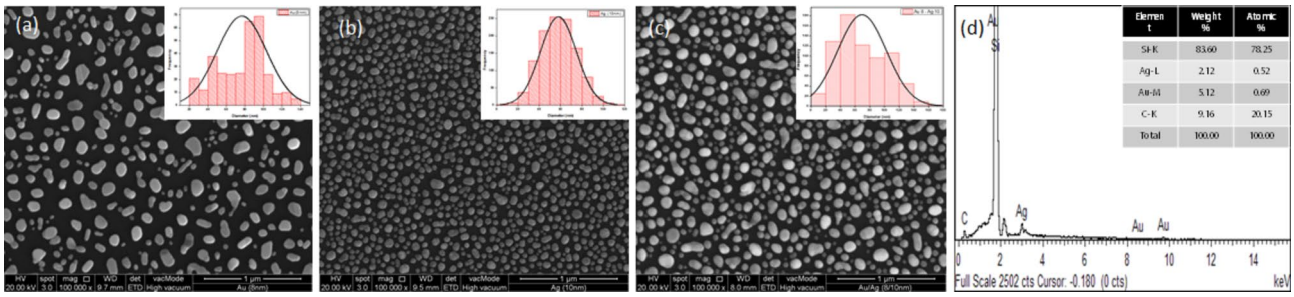

Fig. 3. FESEM images of particle distribution for (**a**) AuNPs, (**b**) AgNPs, (**c**) Au/AgNPs, and (**d**) the EDX spectra for Au/AgNPs formation.

Samples	Coating thickness (nm)	Dominant particles sizes range (nm)	Average particles size (nm)
AuNPs	8	20–140	75
AgNPs	10	20–100	60
Au/AgNPs	8/10	20–180	70

Table 2. Particle size distribution of each nanoparticles.

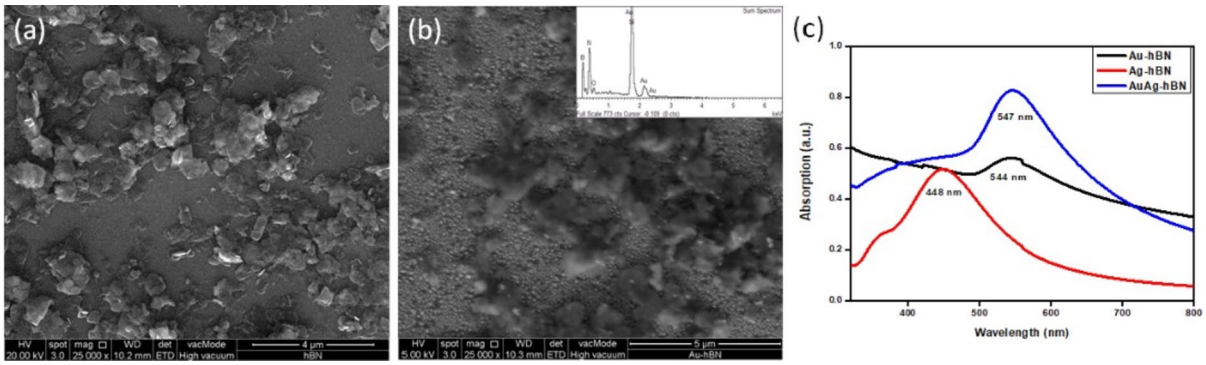

Fig. 4. FESEM images on the formation of hBN on (**a**) Si and (**b**) AuNPs and (**c**) UV-Vis spectra for all photodetector devices.

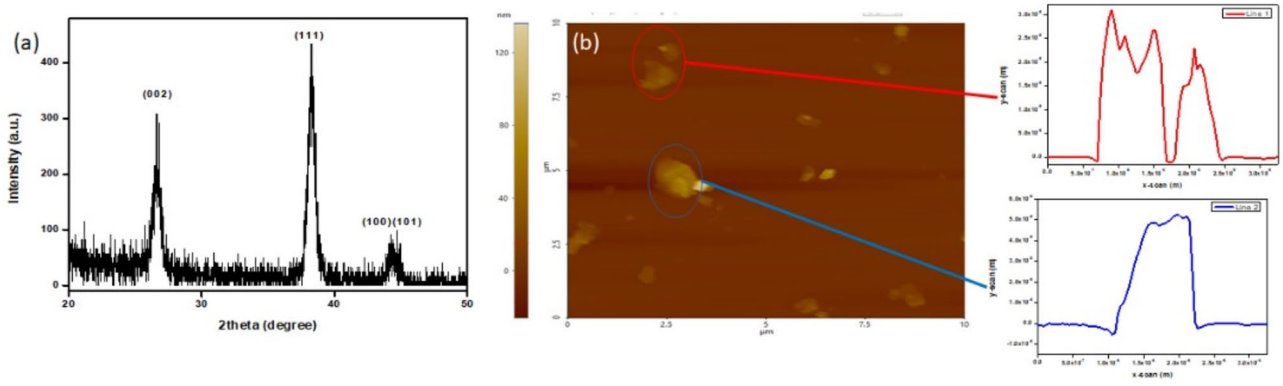

Fig. 5. (**a**) XRD diffraction spectra for hBN and Au NPs and (**b**) AFM topography and line scan for hBN.

exhibits a broader wavelength due to the existence of both AuNPs and AgNPs. This lead to an increase in the oscillation of the particles due to the light-matter interaction in the sample[33].

Figure 5a shows the XRD pattern for the Au-hBN devices with the miller indices of the diffraction given. The main peak at 26.58 °C correspond to the (002) Braggs reflection plane while the peak at 43° to 45° correspond to

unresolved Braggs reflection plane at (100) and (101). From Bragg's Law, the miller of indices of (002) deduced the interlayer distance of d = 0.34 nm[44]. Next, the 38.21° of diffraction peak correspond to the Bragg reflection of (111) of face center cubic. The intense diffraction peak at 38.21° indicate the preferred growth orientation of zero valent gold was fixed in (111) and also indicate a pure Au nanocrystals[45]. Figure 5b shows AFM image was obtained to see observed the topography of the hBN surface. The line scan also was observed within the hBN flakes and shown thickness approximately around 30–50 nm.

Electrical analysis on Au-hBN, Ag-hBN, and Au/Ag-hBN devices

The analysis of the devices was measured using a Keysight Model B2911A source meter with bias ranging from −5 V to +5 V and an SRS Model DS345 function generator to generate different power intensities of the laser. Then, for photo response (I-t), the measurements were taken using a Uni-T MODEL MSO3345E oscilloscope. A 532 nm of light sources were used in this work with the power intensities varying from 0.58 mW/cm^2 to 1.52 mW/cm^2 corresponding to 8.0 V_{pp} to 10.0 V_{pp} of function generator.

The improvement in the performance of the fabricated device under 532 nm light illumination can be explained when the incident light resonates with the plasmonic frequency of the decorated NPs, where a significant number of high-energy electrons generated, forming oscillating electron clouds which commonly referred to as hot electrons, at the surface of the AuNPs known as LSPR[46]. The current-voltage (I-V) measurements were conducted for dark (0 mW/cm^2) and under light illumination varies from 0.58 mW/cm^2 to 1.52 mW/cm^2, which corresponds to the calibration power intensities with an active area of 0.0135 cm^2 which correspond to the laser beam diameter. The measurements were taken under zero bias while source meter bias ranged from −5 V to +5 V. At dark (0 mW/cm^2), all devices exhibit low dark current, 7 µA, 20 µA, and 6 µA for Au-hBN, Ag-hBN, and Au/Ag-hBN devices, respectively, may appear relatively high compared to the low dark current levels (in the range of 10^{-12} to 10^{-10} A) in many advanced photodetectors utilize materials with lower intrinsic dark currents (e.g., silicon or specialized semiconductors like InGaAs)[47]. This work investigates the dark current in hBN-based detectors, highlighting how it can be influenced by the material's intrinsic properties and structure. This work emphasizes while hBN exhibits low intrinsic dark currents, the actual performance can vary significantly depending on device architecture and operating conditions[48]. It is noticeable that the I-V curve for the devices is not symmetrical and the higher value in negative bias for Au-hBN and Au/Ag-hBN is mainly caused by the p-type doped Si substrate used in this work[32].

Figure 6 shows that all devices have an increasing trend of photocurrent when the light power intensities increases from 0.58 mW/cm^2 to 1.52 mW/cm^2 concerning the dark current (0 mW/cm^2). This indicates that the photocurrent is proportional to the light power intensities, which concludes the increase in photo-induced carrier when the number of absorbed photons is increased for all devices. Figure 6a–c, the photoresponse ratio is defined as the ratio of the photocurrent under illumination of 0.58 mW/cm^2 of light power intensities (as red line in the graph) with the photocurrent under dark (as black line in the graph) for all devices. The Au-hBN (Fig. 6a) device exhibits photoresponse ratio of 2.47, while the Ag-hBN (Fig. 6b) and Au/Ag-hBN (Fig. 6c) ratio of 1.38 and 2.16 respectively. The results demonstrate that the Au-hBN device has a higher photo-induced carrier under illumination than the dark current and has high sensitivity at low power densities compared to the other devices.

The photocurrent, $I_{ph} = I_{total} - I_{dark}$, is defined as the net current after deducting the total current under illumination with dark current where I_d is the dark current, and I_{total} is the total current under illumination. Figure 6d, the photocurrent of all devices increased as the power intensities increased. This increases photo-induced carrier within the device as the photon energy increases. Besides, it is shown that the photocurrent for Au-hBN and Ag-hBN devices is higher compared to Au/Ag-hBN devices for all power intensities, indicating higher photo-induced carrier with the existence of monometallic AuNPs and AgNPs compared to bimetallic Au/AgNPs.

The responsivity, $R = I_{ph}/(P_{int} \times A)$, is defined as the sensitivity of the device to generate photocurrent per illuminated optical power, which is calculated using the formula in where I_{ph} is photocurrent, P_{int} is the light power intensities (mW/cm^2), and A is the active area; of 0.0135 cm^2. The decrease in the responsivity in the Au-hBN and Ag-hBN devices at higher light power intensities mainly due to the electron-trap saturation and increasing in the electron-hole recombination[49]. When the traps are filled with electrons, the quasi-Fermi level energy level rises and leads to the increased in the number of free electrons. This result indicates that the Au-hBN and Ag-hBN devices exhibit higher photocurrent generation than the incident photon when illuminated with light at lower intensities.

Figure 7a shows the responsivity of all devices. For the light illumination of 0.58 mW/cm^2, the Au-hBN and Ag-hBN devices show higher responsivity at 1.33 A/W and 1.34 A/W, respectively, compared to Au/Ag-hBN devices that exhibit responsivity of 0.87 A/W at the bias voltage of +5 V. However, Au/Ag shows lower responsivity and EQE compared to AuNPs and AgNPs based photodetector due to the out-phase hybridization which cause the interference effect[32].

Apart from responsivity (R), another crucial parameter of the device performance is the detectivity (D), which is defined as the capability of the device to detect a low signal and is expressed in Eq. (1):

$$D^* = \frac{R \times \sqrt{A}}{\sqrt{2eI_d}} \tag{1}$$

where R is responsivity (in A/W), A is the active area, e is the electron charge, and I_d is the dark current. Figure 7b depicts the detectivity of Au-hBN and Ag-hBN devices with decreasing trend, while the Au/Ag-hBN shows increasing trends with the light power intensities from 0.58 mW/cm^2 to 1.52 mW/cm^2. This indicates that Au-hBN and Ag-hBN devices can detect light at low power density, 0.58 mW/cm^2 compared to Au/Ag-hBN devices. At 0.58 mW/cm^2, the Au-hBN device has a higher detectivity of 1.03×10^{11} Jones, compared to Ag-hBN and

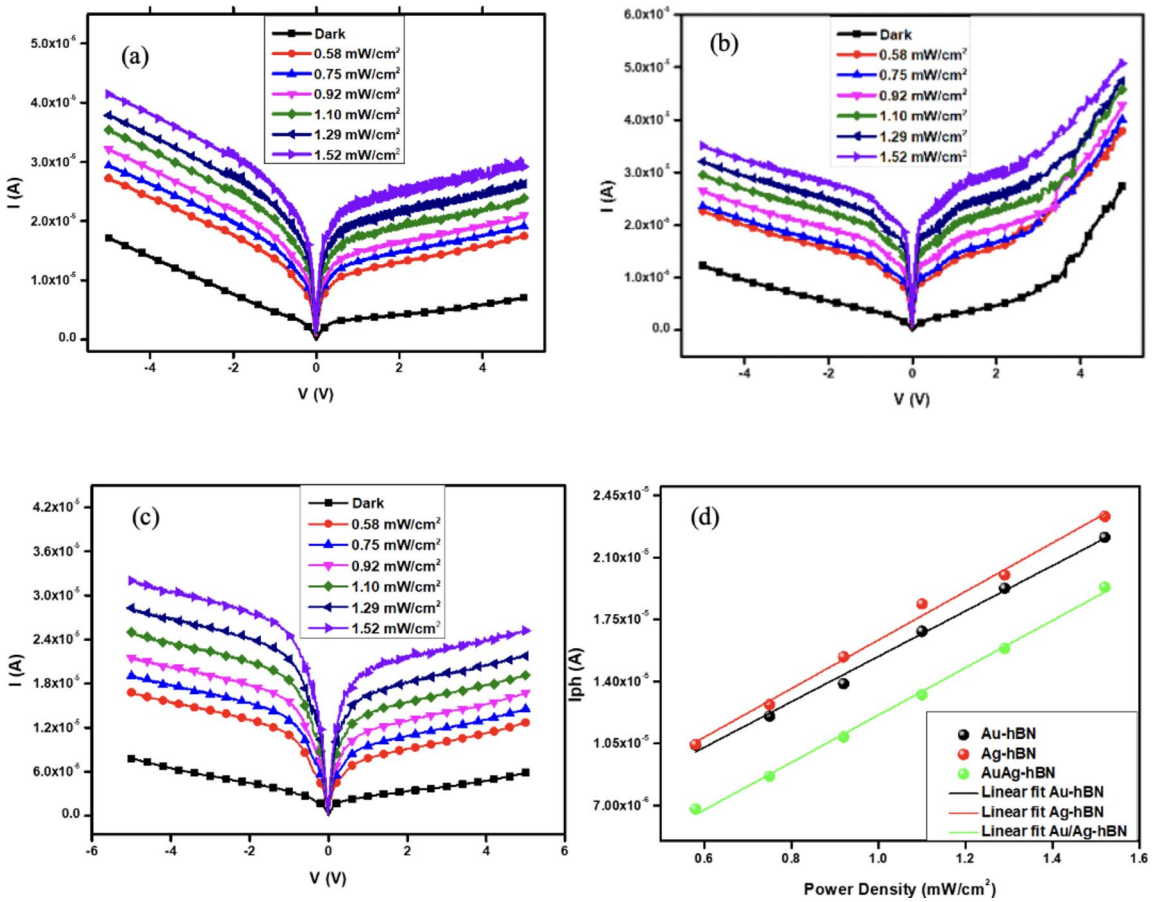

Fig. 6. I-V curve for (**a**) Au-hBN, (**b**) Ag-hBN, (**c**) Au/Ag-hBN photodetector devices. (**d**) The linear fit of the photocurrent of all devices with respect to the light power intensity.

Au/Ag-hBN devices with detectivity of 5.23×10^{10} Jones and 7.35×10^{10} Jones respectively. This deduces that the Au-hBN device has better capability to produce photocurrent at the low signal of light than the other two devices due to the optimum ability of the AuNPs to enhance the light absorption in hBN, which produces more photocurrent.

The parameter associated with the performance of devices is external quantum efficiency (EQE), defined as percentage of the ratio of photocurrent generated per illuminated power by employing the photon energy. It is expressed as in Eq. (2):

$$EQE\,(\%) = \frac{hc}{e} \times \frac{R}{\lambda} \tag{2}$$

where h is the Planck's constant, c is the speed of light, e is the electron charge, R is responsivity, and λ is the incident wavelength. Figure 7c depicts the decreasing trend of EQE upon 0.58 mW/cm^2 to 1.52 mW/cm^2 optical power intensities for the Au-hBN and Ag-hBN devices while increasing the trend for Au/Ag-hBN devices. At the power intensity of 0.58 mW/cm^2, the EQE(%) was found to be 3.10 and 3.11 for Au-hBN and Ag-hBN devices, respectively, while Au/Ag-hBN device exhibited a lower EQE of 2.02. Generally, the higher EQE in Au-hBN and Ag-hBN devices occur due to the enhancement of absorbed photons to more significant plasmonic oscillation of electrons near the surface of AuNPs and AgNPs for both devices, which affected the carrier generation and recombination of the device. From Fig. 7a–c depicts the monometallic of Au-hBN and Ag-hBN devices perform better than Au/Ag-hBN. This indicates better light trapping and carrier recombination within monometallic NPs compared to bimetallic NPs at this wavelength. The summary of the FOM of every device was tabulated in Table 3 shows Au-hBN has highest responsivity of 1.33 A/W, detectivity as 1.03×10^{11} Jones and 245 µs of photo response but slightly lower for EQE than Ag-HBN of 3.11%. The FOM value followed by Ag-hBN which slightly higher for responsivity of 1.34 A/W, lowest detectivity of 5.23×10^{10} Jones and response time of 171 µs. The lowest FOM shows by BMNPSs of Au-Ag with responsivity of 0.87 A/W, lower detectivity of 7.35×10^{10} Jones and response time of 179 µs. The use of bimetallic combinations is aimed at leveraging the complementary properties of the two metals to extend the operational range of the device, due to the interaction between different metal components. This leads to improved light absorption and scattering which are critical for effective photodetection[50]. Specifically, a detailed spectral response study could provide deeper insights into how the bimetallic configuration enhances device functionality across a broader range of wavelengths whereby

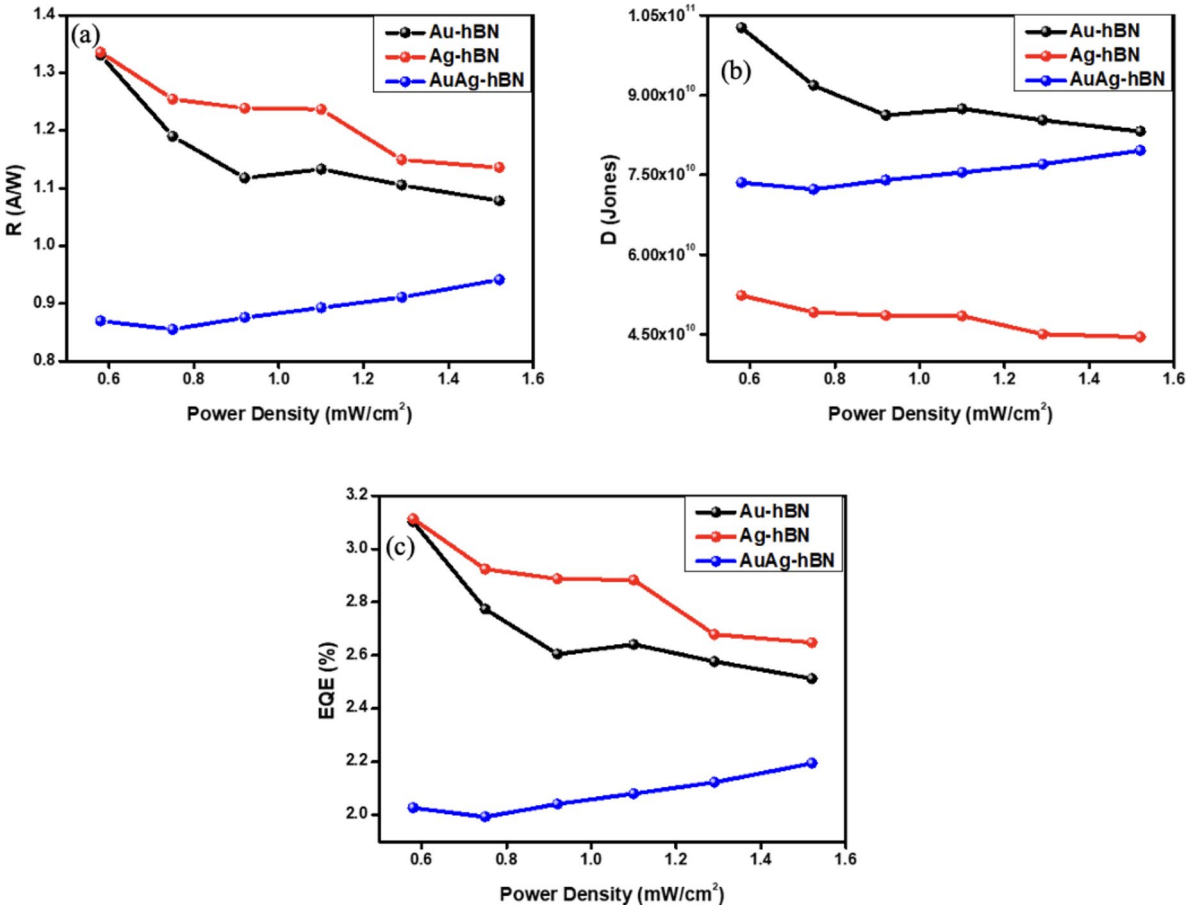

Fig. 7. Figure of merit for (**a**) linear fit of photocurrent, (**b**) responsivity and (**c**) EQE(%) for all photodetector devices.

Device	Responsivity (A/W)	Detectivity (Jones)	EQE (%)	Response time (μs)
Au-hBN	1.33	1.03×10^{11}	3.10	245
Ag-hBN	1.34	5.23×10^{10}	3.11	171
Au/Ag-hBN	0.87	7.35×10^{10}	2.02	179

Table 3. Summary of figure of merit of all devices at 0.58 mW/cm^2 power intensities of 532 nm light.

varying the composition and structure of BMNPs, as it can fine-tune their electronic properties, allowing for optimized performance in specific wavelength ranges which relevant to photodetection[51].

The photo response is based on the rise time of the devices, which is the time required for the device to increase its photocurrent from 10 to 90% of its maximum photocurrent. In Fig. 8, the photoresponse was taken at a power intensity of 1.52 mW/cm^2 and voltage bias of 5 V; Au-hBN shows the longest rise time, 279 μs, which exhibit a rise time of 266 μs and 261 μs, respectively due to the devices enhanced response time from the trapping of the photocarriers[52].

Figure 9 shows all devices with an increasing trend in the response time at high power intensities light. All devices exhibit microsecond response time from low to high light power intensities[53]. Instead of acting as a photoactive material, current research suggests that hBN primarily serves as a charge transport material in various device applications. In the context of this device, hBN primarily serves as a charge transport material rather than a light-absorbing medium. Its role includes facilitating efficient charge transfer between the plasmonic nanoparticles and the metallic contacts, as well as providing a stable interface to minimize recombination losses. The plasmonic nanoparticles, rather than the hBN layer, are primarily responsible for light absorption and generation of hot carriers under this illumination.

This characteristic is crucial in applications requiring stable electronic properties without interference from light-induced excitations and chemical inertness. hBN also can effectively separate conductive layers in heterostructures, reducing leakage currents and enhancing the performance of electronic devices[54,55]. The

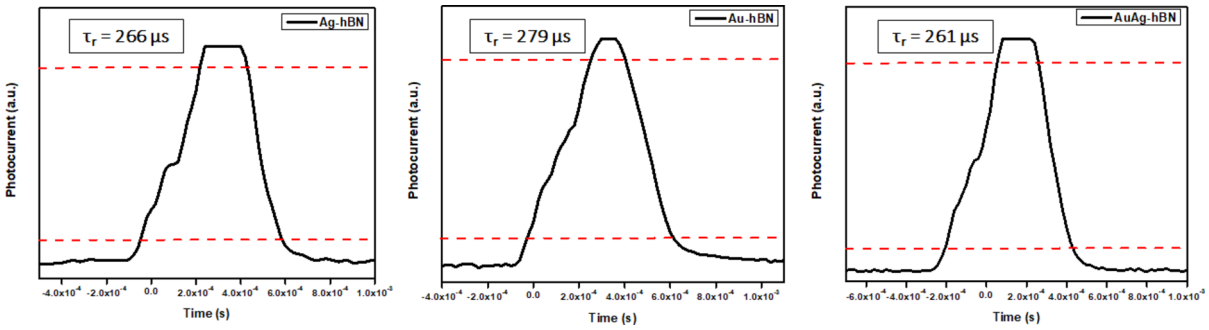

Fig. 8. Photo response of all devices at 1.52 mW/cm^2 of power intensity and voltage bias of 5 V.

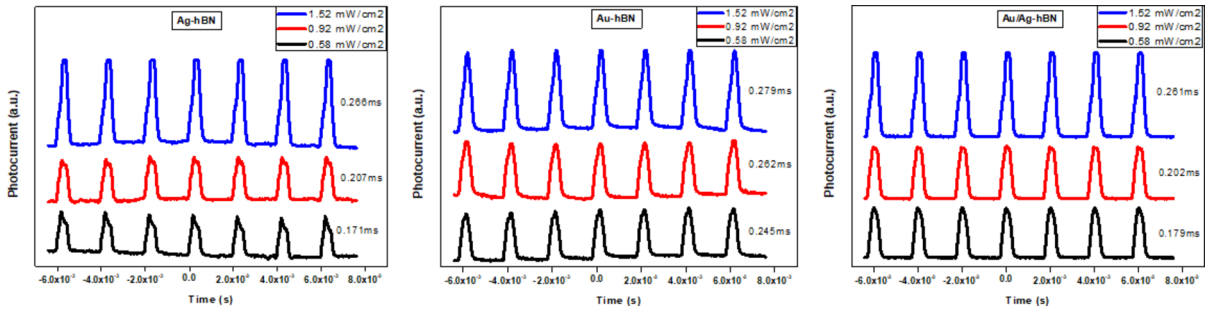

Fig. 9. Photo response of all devices for different power intensities at voltage bias of 5 V.

hBN-based device	Wavelength (nm)	Growth technique /characteristic	Photoresponsivity (mA/W)	Detectivity (Jones)	Response time	References
hBN Nanosheets	254	Short pulse CO_2 laser plasma deposition/bulk layer	1.5	–		56,57
hBN Nanosheets	250	Solid state reaction/multilayer	5.022	6.1×10^{12}	0.2 s	58
Single-crystalline hBN	UV light	Atmospheric Chemical Vapor Deposition (CVD)/ monolayer	5.45	8.62×10^{9}	376, 198 ms	59
hBN nanoflakes	205	Electron beam lithography/multilayer	5.2	–	1.2 s, 6.8 s	60
hBN layer	VUV light	Mechanical exfoliation/multilayer	1000	–	–	61
MoS_2/h-BN/Graphene/Si	532	Wet chemical transfer/multilayer	300	–	10 s	62
Si/Graphene/h-BN/MoS_2	532	CVD/ monolayer	360	6.70×10^{11}	–	63
Al_2O_3/h-BN/Graphene/h-BN/Si	610–1000	Electron beam lithography/multilayer	27	–	17 ns	64
Au-hBN	532	Electron beam evaporation/multilayer	1330	1.03×10^{11}	279 µs	This work
Ag-hBN	532	Electron beam evaporation/multilayer	1340	5.23×10^{10}	266 µs	This work
Au/Ag-hBN	532	Electron beam evaporation/multilayer	870	7.35×10^{10}	261 µs	This work

Table 4. Comparison of current work of h-BN-based photodetector devices with the previous work.

comparison of current work with the previous work on h-BN-based photodetector devices at wavelength of 532 nm was tabulated in Table 4 where shows hBN devices, growth techniques and performance comparison.

Conclusion

In summary, this work presents a novel approach to enhancing photodetector performance through the integration of hBN with plasmonic materials in the visible region (532 nm) which has not been fully explored, particularly in terms of morphology and size control of mono- and bimetallic nanoparticles (BMNPs) namely Au, Ag and Au-Ag; where the selection, optimizing of NPs and photogeneration process will be crucial. The fabricated metallic NPs/hBN photodetector demonstrates a responsivity of 1.33 A/W, a specific detectivity of 1.03×10^{11} Jones, an ultra-low dark current of 7.00 µA with a high photo response ratio of 2.47 highest for Au-hBN photodetector. A Schottky junction-based metal–semiconductor contact configuration is employed to achieve hot-carrier reflections on the metal side, enhancing the quantum efficiency of the device. This improved performance is attributed to the visible light-modulated band-to-band excitation in hBN layer and internal

photoemission resulting from the NPs/hBN junction. This approach of integrating 2D/metal opens possibilities for fabricating low-cost, high-performance and flexible photodetectors in a wide range of optoelectronic devices.

Data availability

The datasets used and analysed during the current study are available from the corresponding author on reasonable request.

Received: 23 October 2024; Accepted: 23 December 2024
Published online: 02 January 2025

References

1. Watanabe, K., Taniguchi, T. & Kanda, H. Direct-bandgap properties and evidence for ultraviolet lasing of hexagonal boron nitride single crystal. *Nat. Mater.* **3**(6), 404–409 (2004).
2. Khan, M. H. et al. Few-atomic-layered hexagonal boron nitride: CVD growth, characterization, and applications. *Mater. Today*. **20**(10), 611–628 (2017).
3. Ogawa, S., Fukushima, S. & Shimatani, M. Hexagonal boron nitride for photonic device applications: a review. *Materials (Basel)* **16**(5) (2023).
4. Merlo, A. et al. Boron nitride nanomaterials: biocompatibility and bio-applications. *Biomater. Sci.* **6**(9), 2298–2311 (2018).
5. Yi, H. et al. Surface etching and edge control of hexagonal boron nitride assisted by triangular sn nanoplates. *Nanoscale Adv.* **4**(18), 3786–3792 (2022).
6. Chen, H. & Zhang, H. *Nano Au-decorated boron nitride nanotubes: Conductance modification and fieldemission enhancement.* (2008).
7. Song, W. L. et al. Polymer/boron nitride nanocomposite materials for superior thermal transport performance. *Angew. Chem. Int. Ed. Engl.* **51**(26), 6498–6501 (2012).
8. Golberg, D. et al. Boron nitride nanotubes and nanosheets. *ACS Nano* **4**(6), 2979–2993 (2010).
9. Cai, Q. et al. High thermal conductivity of high-quality monolayer boron nitride and its thermal expansion. *Sci. Adv.* **5**(6), eaav0129 (2019).
10. Song, S. B. et al. Deep-ultraviolet electroluminescence and photocurrent generation in graphene/hBN/graphene heterostructures. *Nat. Commun.* **12**(1), 7134 (2021).
11. Fukamachi, S. et al. Large-area synthesis and transfer of multilayer hexagonal boron nitride for enhanced graphene device arrays. *Nat. Electron.* **6**(2), 126–136 (2023).
12. Song, S. B. et al. Deep-ultraviolet electroluminescence and photocurrent generation in graphene/hBN/graphene heterostructures. *Nat. Commun.* **12**(7134) (2021).
13. Nerl, H. C. et al. Mapping the energy-momentum dispersion of hBN excitons and hybrid plasmons in hBN-WSe2 heterostructures. *Npj 2D Mater. Appl.* **8**(1), 68 (2024).
14. Wang, P. et al. Plasmonic photocatalysts: harvesting visible light with noble metal nanoparticles. *Phys. Chem. Chem. Phys.* **14**(28), 9813–9825 (2012).
15. Canfarotta, F., Whitcombe, M. J. & Piletsky, S. A. Polymeric nanoparticles for optical sensing. *Biotechnol. Adv.* **31**(8), 1585–1599 (2013).
16. Catchpole, K. R. & Polman, A. Plasmonic solar cells. *Opt. Express* **16**(26), 21793–21800 (2008).
17. Murray, W. A. & Barnes, W. L. Plasmonic materials. *Adv. Mater.* **19**(22), 3771–3782 (2007).
18. Chen, Y. & Ming, H. Review of surface plasmon resonance and localized surface plasmon resonance sensor. *Photonic Sens.* **2**(1), 37–49 (2012).
19. Gupta, B. D., Pathak, A. & Semwal, V. Carbon-based nanomaterials for Plasmonic sensors: a review. *Sensors (Basel)* **19**(16) (2019).
20. Lee, K. S. & El-Sayed, M. A. Gold and silver nanoparticles in sensing and imaging: sensitivity of plasmon response to size, shape, and metal composition. *J. Phys. Chem. B* **110**(39), 19220–19225 (2006).
21. Rogach, A. L. Nanocrystalline CdTe and CdTe(S) particles: wet chemical preparation, size-dependent optical properties and perspectives of optoelectronic applications (2000).
22. Bohren, C. F. & Huffman, D. R. Absorption and scattering of light by small particles (1983).
23. Rodríguez-González, B. et al. Multishell bimetallic AuAg nanoparticles: synthesis, structure and optical properties. *J. Mater. Chem.* **15**(17) (2005).
24. Alissawi, N. et al. Effect of gold alloying on stability of silver nanoparticles and control of silver ion release from vapor-deposited Ag–Au/polytetrafluoroethylene nanocomposites. *Gold Bull.* **46**(1), 3–11 (2012).
25. Gordon, R. et al. A new generation of sensors based on extraordinary optical transmission. *Acc. Chem. Res.* **41**(8), 1049–1057 (2008).
26. Sharma, M. et al. Plasmonic effects of au/ag bimetallic multispiked nanoparticles for photovoltaic applications. *ACS Appl. Mater. Interfaces*. **6**(17), 15472–15479 (2014).
27. Ismail, M. N. S. M. et al. Size-dependent of plasmonic gold nanoparticles enhanced on WS2/Si nanohybrids photodetector. *J. Mater. Sci. Mater. Electron.* **34**(14) (2023).
28. Aroca, R. F. Plasmon enhanced spectroscopy. *Phys. Chem. Chem. Phys.* **15**(15), 5355–5363 (2013).
29. Lim, F. S. et al. Tunable plasmon-induced charge transport and photon absorption of bimetallic Au–Ag nanoparticles on ZnO photoanode for photoelectrochemical enhancement under visible light. *J. Phys. Chem. C* **124**(26), 14105–14117 (2020).
30. Bansal, A., Sekhon, J. S. & Verma, S. S. Scattering efficiency and LSPR tunability of bimetallic Ag, au, and Cu nanoparticles. *Plasmonics* **9**(1), 143–150 (2013).
31. Kunwar, S. et al. Improved photoresponse of UV photodetectors by the incorporation of plasmonic nanoparticles on GaN through the resonant coupling of localized surface plasmon resonance. *Nanomicro Lett.* **12**(1), 91 (2020).
32. Tan, C. L., Lee, S. K. & Lee, Y. T. Bi-SERS sensing and enhancement by Au-Ag bimetallic non-alloyed nanoparticles on amorphous and crystalline silicon substrate. *Opt. Express* **23**(5) (2015).
33. Yang, Y. et al. Preparation of Au–Ag, Ag–Au core–shell bimetallic nanoparticles for surface-enhanced Raman scattering. *Scr. Mater.* **58**(10), 862–865 (2008).
34. Rohizat, N. S. et al. Plasmon-enhanced reduced graphene oxide photodetector with monometallic of au and ag nanoparticles at VIS–NIR region. *Sci. Rep.* **11**(1), 19688 (2021).
35. Frydendahl, C. et al. hBN-encapsulated graphene coupled to a plasmonic metasurface via 1D electrodes for photodetection applications. *Adv. Photonics Res.* **5**(4), 2300192 (2024).
36. Abdullah Ripain, A. H. et al. Highly efficient and stable near-infrared photo sensor based on multilayer MoS2/p-Si integrated with plasmonic gold nanoparticles. *Appl. Phys. Lett.* **123**(6) (2023).
37. Sundararaju, U. et al. MoS2/h-BN/graphene heterostructure and plasmonic effect for self-powering photodetector: a review. *Materials* **14**(7), 1672 (2021).

38. Liu, Y. et al. Plasmon resonance enhanced WS2 photodetector with ultra-high sensitivity and stability. *Appl. Surf. Sci.* **481**, 1127–1132 (2019).
39. Jia, J. et al. Avalanche carrier multiplication in multilayer black phosphorus and avalanche photodetector. *Small* **15**(38), 1805352 (2019).
40. Chen, W. et al. Surface plasmon-enhanced photodetection in MoTe2 phototransistors with au nanoparticles. *Appl. Phys. Lett.* **115**(14) (2019).
41. Gao, L. et al. Low power photodetector based on graphene-WS2-Au structure. *AIP Adv.* **14**(4) (2024).
42. Liu, B. et al. Schottky junction made from a nanoporous au and TiO2 film for plasmonic photodetectors. *ACS Appl. Nano Mater.* **6**(6), 4619–4625 (2023).
43. Mahanta, T., Kasana, P. K. & Mohanty, T. Surface potential mapping of chemically synthesized boron nitride nanosheets. *AIP Conf. Proc.* **2265**(1) (2020).
44. Huang, C. et al. Stable colloidal boron nitride nanosheet dispersion and its potential application in catalysis. *J. Mater. Chem. A* **1**(39) (2013).
45. Krishnamurthy, S. et al. Yucca-derived synthesis of gold nanomaterial and their catalytic potential. *Nanoscale Res. Lett.* **9**(1), 627 (2014).
46. Lim, S. H. et al. Photocurrent spectroscopy of optical absorption enhancement in silicon photodiodes via scattering from surface plasmon polaritons in gold nanoparticles. *J. Appl. Phys.* **101**(10) (2007).
47. Song, B. et al. Low dark current and high speed InGaAs photodiode on CMOS-compatible silicon by heteroepitaxy. *IEEE J. Sel. Top. Quantum Electron.* **28**(2: Optical Detectors), 1–8 (2022).
48. Mballo, A. et al. Natural boron and (10)B-enriched hexagonal boron nitride for high-sensitivity self-biased metal-semiconductor-metal neutron detectors. *ACS Omega* **7**(1), 804–809 (2022).
49. Ismail, M. N. S. M., Ripain, A. H. A., Fahri, M. A. S. A., Zulkifli, N. A. A. & Zakaria, R. Size-dependent of plasmonic gold nanoparticles enhanced on WS2/Si nanohybrids photodetector. *J. Mater. Sci. Mater. Electron.* **34**(1168) (2023).
50. Srinoi, P. et al. Bimetallic nanoparticles: enhanced magnetic and optical properties for emerging biological applications. *Appl. Sci.* **8**(7), 1106 (2018).
51. Larrañaga-Tapia, M. et al. Green synthesis trends and potential applications of bimetallic nanoparticles towards the sustainable development goals 2030. *Nanoscale Adv.* **6**(1), 51–71 (2024).
52. Wang, B. et al. Enhanced current rectification and self-powered photoresponse in multilayer p-MoTe(2)/n-MoS(2) Van Der Waals heterojunctions. *Nanoscale* **9**(30), 10733–10740 (2017).
53. Qiao, S. et al. A vertically layered MoS2/Si heterojunction for an ultrahigh and ultrafast photoresponse photodetector. *J. Mater. Chem. C.* **6**(13), 3233–3239 (2018).
54. Bhimanapati, G. R., Glavin, N. R. & Robinson, J. A. Chapter three—2D boron nitride: synthesis and applications *Semicond. Semimetals* **95**, 101–147 (2016).
55. Novikov, Y. N. & Gritsenko, V. A. The charge transport mechanism in amorphous boron nitride. *J. Non-cryst. Solids* **544**, 120213 (2020).
56. Aldalbahi, A. et al. High-performance and self-powered deep UV photodetectors based on high quality 2D boron nitride nanosheets. *Nanomaterials (Basel)* **7**(12) (2017).
57. Zhou, A. F., Aldalbahi, A. & Feng, P. Vertical metal-semiconductor-metal deep UV photodetectors based on hexagonal boron nitride nanosheets prepared by laser plasma deposition. *Opt. Mater. Express* **6**(10), 3286–3292 (2016).
58. Veeralingam, S. et al. Record-high responsivity and detectivity of a flexible deep-ultraviolet photodetector based on solid state-assisted synthesized hBN nanosheets. *ACS Appl. Electron. Mater.* **3**(3), 1162–1169 (2021).
59. Yang, H. et al. Shape evolution of two dimensional hexagonal boron nitride single domains on Cu/Ni alloy and its applications in ultraviolet detection. *Nanotechnology* **30**(24), 245706 (2019).
60. Kaushik, S., Sorifi, S. & Singh, R. Study of temperature dependent behavior of h-BN nanoflakes based deep UV photodetector. *Photonics Nanostruct. Fundam. Appl.* **43**, 100887 (2021).
61. Zheng, W. et al. Vacuum-ultraviolet photodetection in few-layered h-BN. *ACS Appl. Mater. Interfaces* **10**(32), 27116–27123 (2018).
62. Jeong, H. et al. Metal-Insulator-semiconductor diode consisting of two-dimensional nanomaterials. *Nano Lett.* **16**(3), 1858–1862 (2016).
63. Li, H. et al. Restoring the photovoltaic effect in graphene-based Van Der Waals heterojunctions towards self-powered high-detectivity photodetectors. *Nano Energy* **57**, 214–221 (2019).
64. Castilla, S. et al. Plasmonic antenna coupling to hyperbolic phonon-polaritons for sensitive and fast mid-infrared photodetection with graphene. *Nat. Commun.* **11**(1), 4872 (2020).

Acknowledgements

This work is supported by the Universiti Malaya Research Excellence Grant 2/2024 (Project No. UM-REG038-2024) and Research University Geran (Faculty Programme), Grant number GPF018A-2023.

Disclaimer

The authors certify that they have participated sufficiently in the work to take public responsibility for the content, including participation in the concept, design, analysis, writing, or revision of the manuscript.

Author contributions

MNSMI and MASAF are responsible for writing and experimentation validation. CLT evaluate the technical and findings. RZ supervised and monitored the project. All authors reviewed the manuscript.

Declarations

Competing interests

The authors declare no competing interests.

Additional information

Correspondence and requests for materials should be addressed to C.L.T. or R.Z.

Reprints and permissions information is available at www.nature.com/reprints.

Publisher's note Springer Nature remains neutral with regard to jurisdictional claims in published maps and institutional affiliations.